CrossMark

Magnetic and thermal transport properties of SrFe$_{12}$O$_{19}$ permanent magnets with anisotropic grain structure

A.D. Volodchenkov [a,b,c], S. Ramirez [d,e], R. Samnakay [d,e], R. Salgado [d], Y. Kodera [a,b], A.A. Balandin [c,d,e], J.E. Garay [a,b,c],*

[a] Advanced Material Processing and Synthesis (AMPS) Laboratory, Department of Mechanical and Aerospace Engineering, University of California – San Diego, San Diego, California 92093, United States
[b] Department of Mechanical Engineering, University of California – Riverside, Riverside, California 92521, United States
[c] Spins and Heat in Nanoscale Electronic Systems (SHINES) Center, University of California – Riverside, Riverside, California 92521, United States
[d] Phonon Optimized Engineered Materials (POEM) Center, Department of Electrical and Computer Engineering, University of California – Riverside, Riverside, California 92521, United States
[e] Materials Science and Engineering Program, University of California – Riverside, Riverside, California 92521, United States

HIGHLIGHTS

- We introduce a nano/microstructural design strategy for thermal management of permanent magnets
- The magnets have aligned grains for magnetic performance and increasing thermal conductivity for effective cooling
- The strategy will translate well to other magnetic materials for energy efficient applications such as generators and motors

GRAPHICAL ABSTRACT
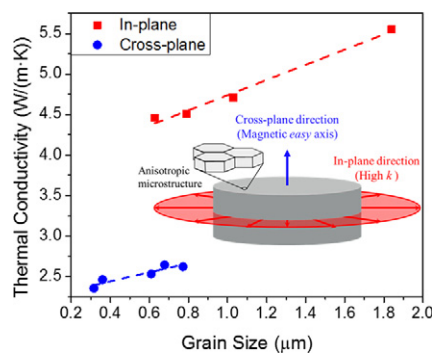
The nano/microstructural design strategy for permanent magnets allows for maximizing magnetic properties, while providing a high thermal conductivity (k) direction for efficient cooling.

ARTICLE INFO

ABSTRACT

Permanent magnets are gaining increasing interest and importance for applications such as generators and motors. Thermal management is a key concern since performance of magnets decreases with temperature. We investigate the magnetic and thermal transport properties of rare earth-free, fine-grained SrFe$_{12}$O$_{19}$ magnets produced by the current activated pressure assisted densification. We propose a cooling scheme based on an anisotropic grain structure that can help retain magnetic performance under high temperature conditions. The synthesized magnets have aligned grains such that their magnetic easy axis is perpendicular to their largest surface area to maximize their magnetic performance. The SrFe$_{12}$O$_{19}$ magnets have fine grain sizes in the cross-plane direction and substantially larger grain sizes in the in-plane direction. This microstructure results in approximately a factor of two higher thermal conductivity in the in-plane direction, providing an opportunity for effective cooling. The phonons are the dominant heat carriers near room temperature. Temperature and direction dependent thermal conductivity measurements indicate that both Umklapp and grain boundary scattering are important in the in-plane direction, while grain boundary scattering dominates the cross-plane thermal transport.

* Corresponding author at: Advanced Material Processing and Synthesis (AMPS) Laboratory, Department of Mechanical and Aerospace Engineering, University of California – San Diego, San Diego, California 92093, United States.
E-mail address: jegaray@ucsd.edu (J.E. Garay).

The proposed design strategy should translate well to other material systems and has important implications for thermal management of nanostructured permanent magnets.

1. Introduction

Permanent magnets (PMs) are used in a wide variety of applications ranging from power sources to switches and actuators [1,2]. Today, high-performance sintered [3] and fine grained sized [4] are playing an increasingly important role in electric motors and generators [5,6] since PM based designs are usually more efficient than traditional electro-magnet based designs because they do not require external power to generate the requisite magnetic field. In addition, PM based energy generating systems are typically more compact and require less maintenance, and therefore offer lower operational costs than traditional motors and generators.

Despite these promising attributes, there are fundamental problems with the generators and motors that use PMs. The first is the large amounts of PM material – sometimes kg quantities – which are needed for intended applications. Currently, the best PMs rely on rare earth elements whose supply chain in uncertain [1]. One of the most promising strategies for reducing the rare earth content is using the exchange spring concept [7–10] that requires nanostructuring of the PM material. This dovetails into the second problem, which is the need for thermal management, since generator and motors generate heat and thus operate at elevated temperatures [11]. PM performance is well known to decrease with temperature, ultimately disappearing at the Curie temperature, T_c. A solution to retaining the magnetic performance could be an active cooling of the magnets. However, nanostructuring reduces cooling efficiency since the abundance of interfaces in nanostructured materials significantly lowers the thermal conductivity, k, of materials [12,13].

Here, we propose a strategy based on aligned, high aspect ratio grains that allows for nanostructured grains in one direction, while still providing a high k path for efficient cooing. Fig. 1a illustrates the benefits of an anisot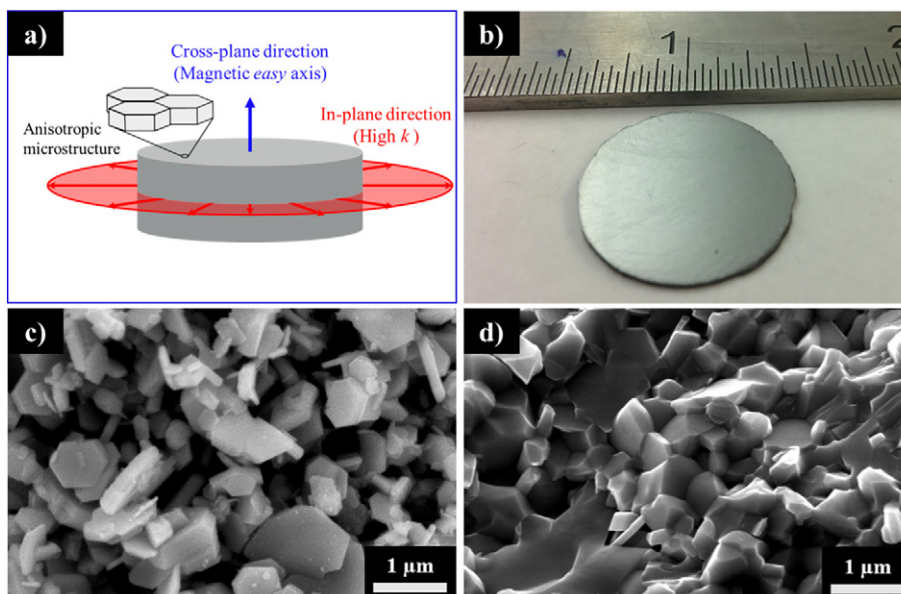ropic, high aspect ratio microstructure. Magnets with grains aligned in such a way that their easy magnetic axis is along the cross-plane, will produce high magnetic field, allowing for stacking of magnets and maximizing surface area of magnetization. Larger grain sizes in the in-plane direction ensure fewer grain boundaries and longer mean free path for heat carriers, maximizing k. In order to test these ideas, we produced fine grain sized permanent magnets using current activated pressure assisted densification (CAPAD) that has been shown to be a viable approach for producing nanostructured magnets [14]. We chose to use strontium ferrite, $SrFe_{12}O_{19}$, henceforth referred to as SFO as a model PM system because of its abundance, low toxicity and high usage in consumer devices [2,15]. SFO is an actively studied [16] hard magnet with a hexagonal magneto-plumbite structure, having a relatively large anisotropy constant and easy magnetic axis perpendicular to the basal plane.

In the rest of the paper we describe the magnetic and thermal properties of fine grained SFO. In addition to facilitating the proposed cooling strategy, the produced high aspect ratio, anisotropic samples provide an efficient platform for evaluating the effects of grain sizes and porosity on thermal conductivity of this class of materials. Specifically, they allowed us to explore thermal transport in materials with two different length scales but with the same global porosity and the same chemical and phase composition. We used Laser Flash and Hot Disk methods, proven transient techniques for measuring thermal diffusivity and thermal conductivity of bulk materials.

2. Experimental procedures

2.1. Material synthesis and processing

In order to investigate the effect of porosity and grain size on the magnetic and thermal properties of PM materials, nano-scale ceramic magnetic powder was densified into bulk samples using CAPAD

Fig. 1. a) A schematic of the high aspect ratio microstructure of permanent magnets. The magnetic easy axis is aligned cross-plane, maximizing surface area in the highest magnetization direction. Larger grain sizes in the in-plane direction enhance the thermal conductivity. b) An optical image of CAPAD processed SFO magnet. The sample dimensions are 19 mm in diameter and ~1.5 mm in thickness. c) A micrograph of the starting SFO powder. The powder particles are relatively loose flakes with the high aspect ratio. d) A micrograph of a fracture surface of a typical CAPAD processed SFO magnet.

technique which is often referred to as Spark Plasma Sintering (SPS) or Field Assisted sintering technique (FAST). Commercial SFO powder with the reported 500 nm particle size (Nanostructured & Amorphous Materials Inc.) was loaded into a graphite die and plunger (19 mm inner diameter) assembly. Mechanical load and current was simultaneously applied in order to achieve heating rates up to ~300 °C/min and mechanical pressure up to 140 MPa. Holding temperatures were between 800 °C and 1000 °C. The mass density of the samples, ρ, was measured geometrically and relative density, ρ_{rel}, was found using the theoretical density of SFO, 5.1 g/cm^3.

2.2. Microstructural characterization

Fracture surfaces of densified samples were examined by the scanning electron microscopy (SEM). The grain size was derived from SEM (Philips XL-30) inspection using an accelerating voltage of 10 kV and working distance of 10 mm. The average grain size, d, was measured by averaging direct grain measurements of over 100 grains per sample taken from SEM micrographs using image processing software (ImageJ). Since the produced SFO has high anisotropy, two length measurements were taken per grain to achieve a more accurate average. The two grain size measurements per grain resulted in an average radial and axial grain size. The crystallographic phase characterization was done by X-ray diffraction (XRD) using a PANalytical Empyrean Diffractometer with Cu Kα X-ray source $\lambda_{K\alpha1} = 1.54056$ Å $\lambda_{K\alpha2} = 1.54440$ Å using 0.01313° step size.

2.3. Magnetic measurements

Magnetic hysteresis loops were measured using a Vibrating Sample Magnetometer (VSM) (Lakeshore 7400 Series) at room temperature. The external field values of up to 1.7 T were applied in order to attain the volume normalized magnetization, M [emu/cm^3] vs. applied field, H [Oe]. Magnetic induction B [G] was calculated using the relation $B = H + 4\pi M$. The sample was rotated in the magnetic field in order to attain M vs. H hysteresis loops at varying angle, θ. A Cube sample shape was used to negate geometrical influences on magnetic measurements and ensure varying θ measurements are comparable.

2.4. Thermal measurements

The CAPAD processed cylindrical samples with diameter of 19 mm and thickness of ~1.5 mm were cut into cubes of dimensions ~12 mm × 13 mm × 1.5 mm. The Laser Flash method was used for cross-plane thermal diffusivity and conductivity measurements, while the Hot Disk technique was used for in-plane thermal diffusivity and conductivity measurements.

2.4.1. Laser Flash

The cut samples were thinly coated with a graphite spray to help with transmittance of laser light and placed inside the LFA 447 instrument. The Laser Flash method is a transient method for measuring thermal diffusivity and operates by using a flash lamp as a heating source. The flash lamp heats one side of the sample while an InSb IR detector records the samples' backside temperature rise. The temperature rise is converted into an electrical signal and is used to calculate the thermal diffusivity, α of the sample. Thermal conductivity, k is calculated using $k = \alpha\rho C_p$, where C_p is the specific heat of the sample and ρ is the density of the sample. The specific heat is measured separately using comparison with the sample with the known tabulated C_p. The cross-plane thermal conductivity was measured from 20 °C to 100 °C. Details of the Laser Flash measurement procedures have been reported by some of us elsewhere [17,18].

2.4.2. Hot Disk

The Hot Disk method is a transient method that allows one to simultaneously determine the thermal diffusivity and thermal conductivity [19]. The methods uses a sensor placed inside two sufficiently large pieces of a material under test. A constant pressure was applied during the measurements to minimize the influence of possible air gaps between the sensor and sample surfaces. The thermal characteristics are extracted from the temperature rise as a function of time recorded during the measurement. The physical principles and formulas for calculating the thermal diffusivity and thermal conductivity from the measured transient data can be found in Refs [20–22].

3. Results and discussion

Fig. 1b shows an optical image of a typical CAPAD processed magnet next to a ruler. The samples are 19 mm in diameter and ~1.5 mm in thickness. A micrograph of the starting powder is shown in Fig. 1c. The powder particles are relatively loose flakes with high aspect ratio. Average flake thickness (axial dimension) is 0.16 μm while average flake length (radial dimension) is 1.12 μm. Some particles are good examples of hexagonal prisms, which relates well to the hexagonal magneto-plumbite structure of SrFe$_{12}$O$_{19}$. Fig. 1d is a micrograph of a fracture surface of a typical CAPAD processed magnet.

In order to examine the role of average grain size, d and porosity, $P = 1 - \rho_{rel}$, we made two sets of samples. The first set has similar ρ_{rel} (94.5% to 96.4%) with a range in d (radial = 0.63 μm to 1.84 μm); the second had similar d (radial = 0.63 to 0.78) but a range in ρ_{rel} (86% to 96%). These two sets of samples are identified with shaded regions in Fig. 2a, which plots average radial and axial grain sizes vs. ρ_{rel} for the SFO samples.

In Fig. 2b we present XRD data for the starting SFO powder, representative densified SFO samples (950 °C, 104 MPa, 1 min hold) and
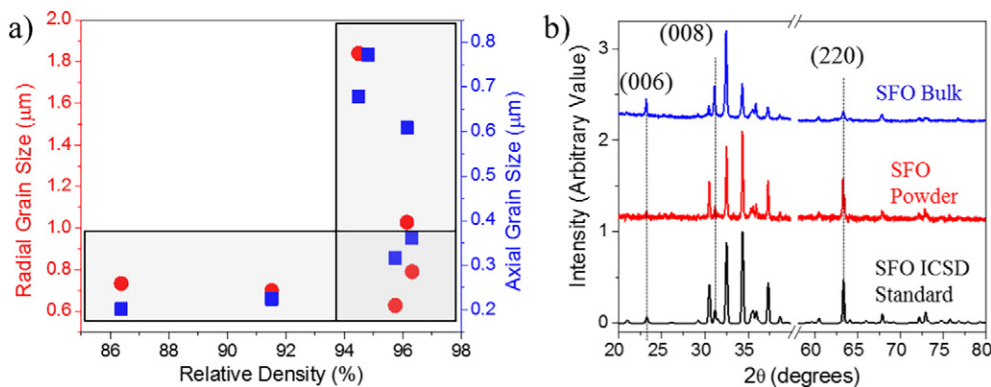
Fig. 2. Microstructural characteristics of CAPAD processed SFO samples. a) The average radial and axial grain sizes vs. relative density. b) XRD profiles for the starting SFO powder and a representative densified SFO sample (950 °C, 104 MPa, 1 min hold). The profile of ICSD standard (#202518) is plotted for comparison. Comparison of the XRD profiles reveals preferential orientation of the planes in the bulk sample.

SFO ICSD standard (#202518). This ICSD standard was measured on randomly oriented powder produced by conventional routes, making representative of sample with randomly oriented grains. All XRD peaks in the powder, as well as densified samples, correspond to SFO, indicating no second phases in the starting powder and no detectable reaction in the CAPAD process. Comparison of the XRD peak intensities however does reveal preferential orientation of planes. The relative intensities of peaks of the randomly oriented powder match those of the ICSD standard while the XRD peak intensities of the densified SFO peaks differ in relative intensity. The peak intensities, which correspond to the (00X) planes such as (006) and (008) increase, while those that correspond to (XX0) peaks decrease in intensity. Materials with the hexagonal symmetry often have preferential growth directions so that the high aspect ratio flakes are formed. Recent results of microwave sintering of SFO and doped SFO do not show evidence of alignment by XRD [23]. We attribute the preferential alignment in our samples to a combination of the high aspect ratio of the starting SFO powder flakes and preferential growth of grains during the CAPAD processing. The result is samples with a high aspect ratio grain morphology with larger grains in the in-plane direction compared to the cross-plane direction as mentioned before.
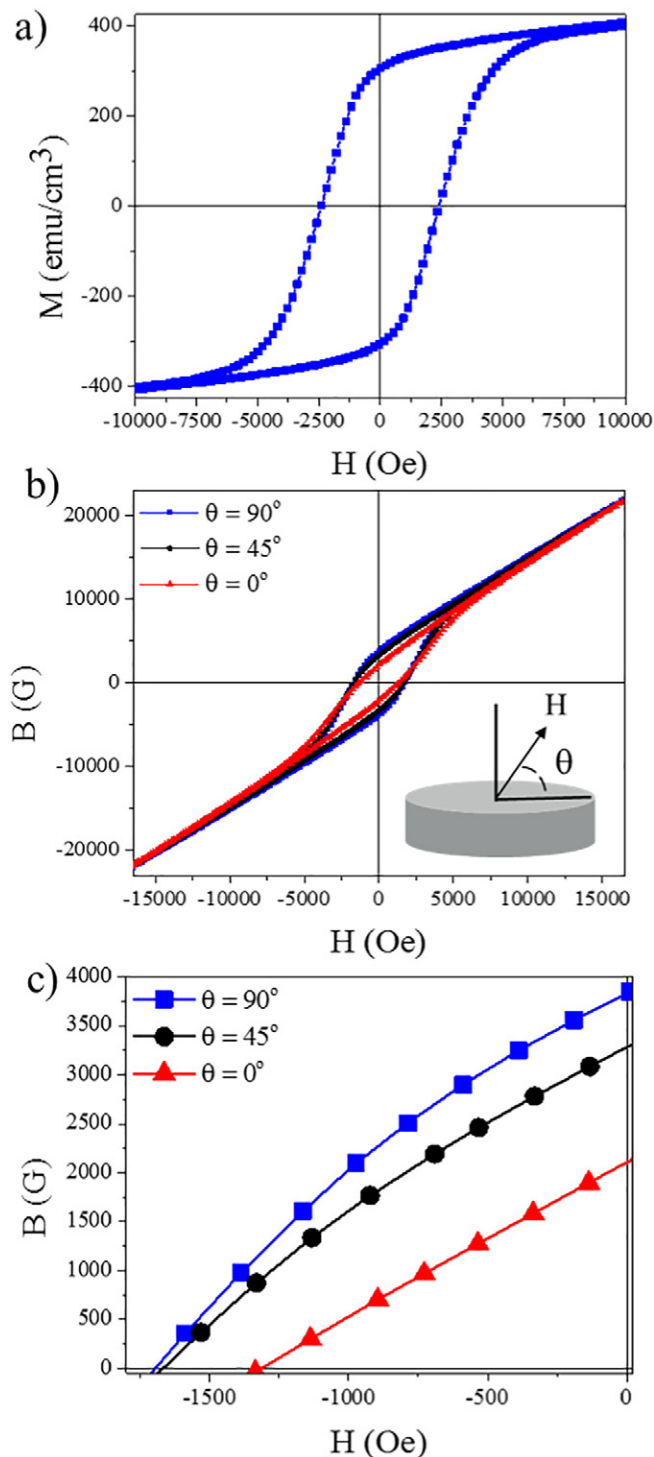
Magnetic hysteresis loop of a typical densified SFO (densified at 1000 °C) measured with H in the cross-plane direction is shown in Fig. 3a. The M-H curve is relatively square as expected for a hard magnetic material showing some degree of alignment. The energy product of the sample is $(BH)_{max} = 1.02$ MGOe which is in the range expected for a SFO ferrite magnet. The coercive field, H_c, is 2460 Oe. The magnetic saturation, M_s, which is calculated by subtracting the non-saturating slope (SFO is ferrimagnetic), is 380 emu/cm^3. The remnant magnetization, M_r, is 310 emu/cm^3. This yields an M_r/M_s ratio of 0.82, which is higher than 0.5 maximum for the expected isotropic magnets without grain alignment [24]. For example, Pullar et al. obtained an $M_r/M_s = 0.49$ for a randomly oriented SFO sintered at 1000 °C with grain sizes that ranged from 0.3 to 1 μm [25].

In order to further corroborate the XRD results that indicate preferential grain orientation, we conducted angle dependent magnetic measurements by varying the angle, θ between the magnetic field, H and samples' in-plane direction as shown in inset of Fig. 3b. Fig. 3b and c show the B-H hysteresis curves (no demagnetization factor was used) as a function of angle, θ. A clear difference is observed in the B-H curves as the hysteresis loop is measured at different H orientations relative to the sample (θ = 0° (H in-plane), θ = 45° and θ = 90° (H cross-plane)). We used a cube of material allowing us to ensure no size/geometry effects or shape contributions to the magnetic measurement, which is confirmed by the samples having the same saturation magnetic induction, B_s. The measurements with H out-of-plane produces the largest remnant magnetic induction, B_r, followed by H 45° to plane and lastly by H in-plane at 3840 G, 3280 G and 2100, respectively. The corresponding remnant volume magnetization values are $M_r = 310$ emu/cm^3 at θ = 0° (H in-plane), $M_r = 260$ emu/cm^3 at θ = 45° and $M_r = 170$ emu/cm^3 θ = 90° (H cross-plane)). These measurements show that the in-plane M_r is almost twice that of the cross plane M_r. The H_c from the B-H loop has a similar trend with H out-of-plane highest, followed by H 45° to plane and lastly by H in-plane at 1710 Oe, 1660 Oe and 1320 Oe, respectively. These measurements prove that the samples have preferentially oriented grains and that the easy axis of magnetization is in the cross-plane (θ = 90°) direction. Knowing that the easy axis of SFO is perpendicular to the basal plane, we conclude that the grains are oriented with basal plane preferentially oriented along the in-plane sample direction while the c-axis is in the cross-plane direction.

Electrical conductivity was measured for the samples processed at 800 °C and 1000 °C to determine whether phonons or electrons are the dominant contributors to heat conduction. The electrical conductivities for the samples processed at 800 °C and 1000 °C were 1.98×10^{-7} Ω^{-1}-cm^{-1} and 3.1×10^{-6} Ω^{-1}-cm^{-1},

respectively. The electron contribution to the thermal conductivity was calculated using the Wiedemann-Franz law. It was determined to be 1.45×10^{-10} W/(m·K) and 2.28×10^{-9} W/(m·K), respectively. Such a low contribution signifies that phonons are the dominant heat carriers in SrFe$_{12}$O$_{19}$.

Fig. 4 shows the temperature dependence of thermal diffusivity (Fig. 4a and b) and thermal conductivity (Fig. 4c and d) in the in-


Fig. 3. Magnetic properties of CAPAD processed SFO magnets. a) Magnetic hysteresis loop of a typical densified SFO (densified at 1000 °C) measured with H in the cross-plane direction. b) B-H hysteresis curves as a function of the measurement angle, θ. The inset shows the relation between θ and the surfaces of the magnets. Note: cubes of material cut from disk shaped samples were used in measurement. c) A magnification of the B-H measurements in the second quadrant, clearly showing orientation effects.
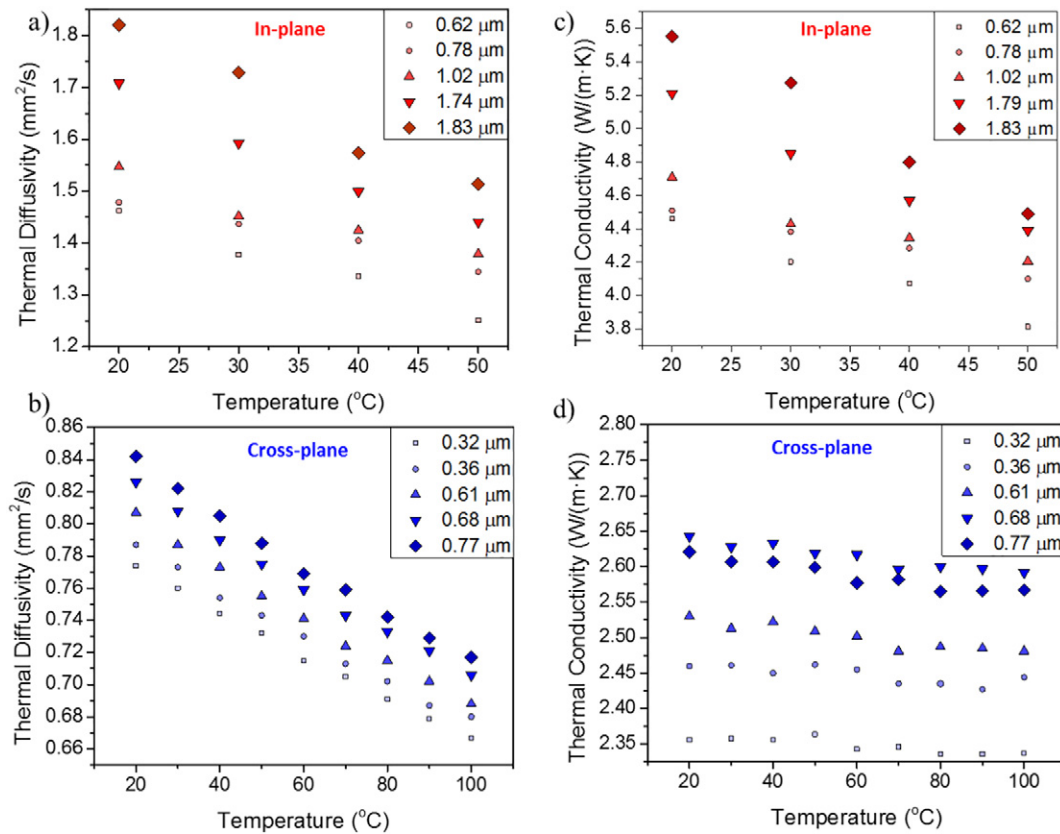
Fig. 4. Thermal properties of CAPAD processed SFO magnets with similar relative densities: a) thermal diffusivity in the in-plane direction; b) thermal diffusivity in the cross-plane direction; c) thermal conductivity in the in-plane direction; d) thermal conductivity in the cross-plane direction.

plane and cross-plane directions for the set of samples with similar densities. The data correspond to the samples with various grain sizes. Note that the radial grain size is the characteristic grain size for the in-plane measurements while the axial grain size is used for the cross-plane. The in-plane measurements show decreasing thermal conductivity with temperature. For example, the decrease for the largest grain size sample (1.8 μm) is ~20% over this temperature range. This suggests that the thermal conductivity is limited to a large degree by the phonon Umklapp scattering in the in-plane direction. Umklapp scattering is an intrinsic phonon scattering mechanism originating from the crystal lattice inharmonicity. It is characterized by ~1/T dependence of the thermal conductivity on temperature [26,27]. By contrast, the cross-plane

thermal conductivity does not change significantly (>2%) over this temperature range for all samples. Since the composition of the magnets does not change with measurement direction, these results suggest that grain boundary scattering is dominant scattering mechanism in the cross-plane direction. The boundary scattering becomes significant when the size of the structure becomes less than the intrinsic phonon mean free path [26,27]. In this case, the phonons do not travel far enough to encounter scattering from other phonons. Instead, they are scattered by the grain boundaries. The phonon transport regime dominated by the boundary scattering is characterized by a weak temperature dependence of the thermal conductivity. A larger number of grain boundaries in the cross-plane direction can also play a role in the
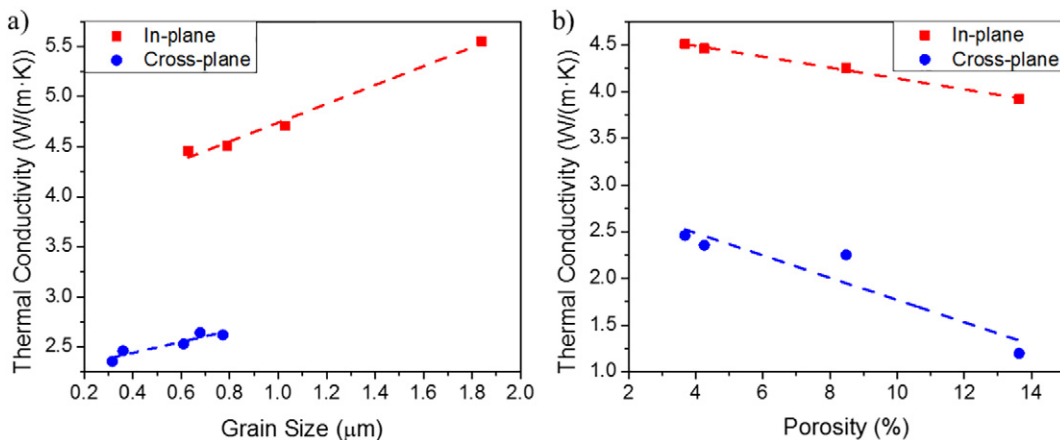
Fig. 5. a) The dependence of thermal conductivity on grain size for samples with similar relative density in the in-plane and cross-plane direction. b) The dependence of thermal conductivity on porosity for samples with the similar grain size in the in-plane and cross-plane direction.

measured thermal characteristics. The direction-dependent phonon thermal transport in our samples can be explained by the difference in the axial and radial grain sizes, with the latter being ~2–2.5 times larger than the former.

The anisotropy in the grain sizes also causes a significant change in the magnitude of the k which ranges from 5.6 to 4.4 W/(m·K) for the in-plane and 2.65 to 2.25 W/(m·K) for the cross-plane direction at room temperature. This degree of anisotropy is comparable to advanced composites based on alignment and microstructural length scale control to control thermal conductivity [28] The dependence of the thermal conductivity on the grain size for the samples with similar ρ_{rel} can be seen in Fig. 5a. The linear best fit lines are also plotted. The fit is good for the in-plane direction ($R^2 = 0.98$) and adequate for the cross-plane direction ($R^2 = 0.84$). The data show that the grain size dependence is stronger in the in-plane direction. The slope of the linear fit is nearly twice the cross-plane slope (0.94 for in-plane compared to the cross-plane slope, 0.55). A linear grain size dependence of k (power law $k \propto d^1$) suggests the strong effect of the phonon – boundary scattering on heat conduction. The data of Fig. 5 together with Fig. 4 indicate that both Umklapp and grain boundary scattering are important in the in-plane direction while grain boundary scattering dominates in the cross-plane direction.

Fig. 5b shows the thermal conductivity dependence on porosity for the set of samples with comparable grain sizes. As expected, the thermal conductivity decreases with porosity. The linear best fit lines are plotted and, again, the fit is better for in the in-plane direction ($R^2 = 0.99$) and adequate in the cross plane ($R^2 = 0.82$). For this set of samples, the porosity dependence is larger for the cross-plane direction. The slope of the line is −0.12 compared to −0.06 for in the in-plane direction. It is interesting to compare this porosity dependence with a classical theory for thermal conductivity in porous samples (Eucken model). It is known that the thermal conductivity of porous materials, k_p, can be written as [29,30]:

$$k_p = k_s \frac{1 + 2P\dfrac{1-Q}{2Q+1}}{1 - P\dfrac{1-Q}{2Q+1}} \tag{1}$$

where P is the volume pore fraction, k_s is the thermal conductivity of the non-porous solid and Q is the ratio of k_s to air ($Q = k_s/k_a$). In the case when Q is relatively large, i.e. the thermal conductivity of the solid is large compared to air, Eq. (1) can be well approximated as linear over the considered porosity range. Using $k_s = 5.6$ W/(m·K) for SFO and 0.0257 W/(m·K) for air, the slope in our porosity range given by Eq. (1) is −0.07 which is very close to −0.06 we measured in the in-plane direction. In the cross-plane direction the slope (−0.12) is almost twice the predicted slope. This means that the classical theory, expressed by Eq. (1), captures the porosity dependence accurately when the characteristic grain size is relatively large (as in the in-plane direction in our samples). However, this theory underestimates the effect of porosity when the characteristic grain size is in the nanometer to sub-micrometer range. The latter can be attributed to the strong phonon boundary scattering effects in the samples with smaller grain sizes. Similar discrepancy between the experiments and classical theory of the effects of porosity has been observed before in nanocrystalline samples synthesized by the same CAPAD technique [13].

The obtained results have important implications for practical application of permanent magnets. As mentioned previously, PMs are being increasingly used in environments where they are exposed to elevated temperatures, which decrease the magnetization. The anisotropy of a magnet can be used to optimize both magnetic performance and provide an effective direction for heat removal. The magnet will provide the highest magnetic field along the easy axis (as demonstrated in Fig. 3), which in the example here is in the cross-plane direction. In order to maintain the temperature as low as possible, and maintain the best magnetic performance, one should cool the PM in the in-plane direction (along directions of largest grains), since the thermal conductivity is about twice the cross plane direction (as demonstrated in Fig. 4). While anisotropic thermal conductivity has recently received attention for thermal management in polymer [31,32] and metal [33,34] based composites this strategy has not been leveraged in permanent magnets.

4. Conclusions

In summary, we produced dense SFO magnets that have high aspect ratio grain morphology resulting in preferential alignment of crystallographic planes. The magnets have the magnetic easy axis aligned perpendicular to their largest surface area (cross-plane) to maximize their magnetic performance. They have higher thermal conductivity in the in-plane direction providing opportunity for effective cooling. Temperature and direction dependent thermal conductivity indicate that both Umklapp and grain boundary scattering are important in the in-plane direction (with relatively large characteristic grain size) while grain boundary scattering dominates in the cross-plane direction (with relatively small characteristic grain size). These results should translate well to other nanostructured permanent magnets (for example those based on the exchange spring concept) and thus have important implications of the thermal management of permanent magnets in demanding applications such as generators and motors.

References

[1] N. Jones, The pull of stronger magnets, Nature 472 (2011) 22–23.
[2] N. Poudyal, J. Ping Liu, Advances in nanostructured permanent magnets research, J. Phys. D. Appl. Phys. 46 (2013) 043001–043023.
[3] Q. Zhou, Z.W. Liu, X.C. Zhong, G.Q. Zhang, Properties improvement and structural optimization of sintered NdFeB magnets by non-rare earth compound grain boundary diffusion, Mater. Des. 86 (2015) 114–120.
[4] L.Z. Zhao, Q. Zhou, J.S. Zhang, D.L. Jiao, Z.W. Liu, J.M. Greneche, A nanocomposite structure in directly cast NdFeB based alloy with low Nd content for potential anisotropic permanent magnets, Mater. Des. 117 (2017) 326–331.
[5] H. Li, Z. Chen, H. Polinder, Optimization of multibrid permanent-magnet wind generator systems, IEEE Trans. Energy Convers. 24 (2009) 82–92.
[6] Huawei Zhou, Zhen Lu, Wenxiang Zhao, Guohai Liu, Liang Xu, Design and analysis of low-cost tubular fault-tolerant interior permanent-magnet motor, IEEE Trans. Magn. 52 (2016) 8104804.
[7] X. Wen, J.S. Andrew, D.P. Arnold, Exchange-coupled hard magnetic Fe-Co/CoPt nanocomposite films fabricated by electro-infiltration, AIP Adv. 7 (2017) 056225.
[8] B. Balamurugan, D.J. Sellmyer, G.C. Hadjipanayis, R. Skomski, Prospects for nanoparticle-based permanent magnets, Scr. Mater. 67 (2012) 542–547.
[9] R. Skomski, J.M.D. Coey, Giant energy product in nanostructured two-phase magnets, Phys. Rev. B 48 (1993) 15812–15816.
[10] A.D. Volodchenkov, Y. Kodera, J.E. Garay, Synthesis of strontium ferrite/iron oxide exchange coupled nano-powders with improved energy product for rare earth free permanent magnet applications, J. Mater. Chem. C 4 (2016) 5593–5601.
[11] N. Zhao, Z.Q. Zhu, W. Liu, Rotor eddy current loss calculation and thermal analysis of permanent magnet motor and generator, IEEE Trans. Magn. 47 (2011) 4199–4202.
[12] S. Ghosh, D. Teweldebrhan, J.R. Morales, J.E. Garay, A.A. Balandin, Thermal properties of the optically transparent pore-free nanostructured yttria-stabilized zirconia, J. Appl. Phys. 106 (2009) 113507.
[13] Z. Wang, J.E. Alaniz, W. Jang, J.E. Garay, C. Dames, Thermal conductivity of nanocrystalline silicon: importance of grain size and frequency-dependent mean free paths, Nano Lett. 11 (2011) 2206–2213.
[14] J.R. Morales, S. Tanju, W.P. Beyermann, J.E. Garay, Exchange bias in large three dimensional iron oxide nanocomposites, Appl. Phys. Lett. 96 (2010) 013102.
[15] K.J. Strnat, Modern permanent magnets for applications in electro-technology, Proc. IEEE 78 (1990) 923–946.
[16] D. Chen, Y. Meng, K.H. Gandha, D. Zeng, Hongya Yu, J. Ping Liu, Morphology control of hexagonal strontium ferrite micro/nano-crystals, AIP Adv. 7 (2017) 056214.
[17] R. Gulotty, M. Castellino, P. Jagdale, A. Tagliaferro, A.A. Balandin, Effects of functionalization on thermal properties of single-wall and multi-wall carbon nanotube polymer nanocomposites, ACS Nano 7 (2013) 5114.

[18] P. Goli, H. Ning, X. Li, C.Y. Lu, K.S. Novoselov, A.A. Balandin, Thermal properties of graphene - copper - graphene heterogeneous films, Nano Lett. 14 (2014) 1497.

[19] P. Goli, S. Legedza, A. Dhar, R. Salgado, J. Renteria, A.A. Balandin, Graphene-enhanced hybrid phase change materials for thermal management of Li-ion batteries, J. Power Sources 248 (2014) 37.

[20] S.E. Gustafsson, Rev. Sci. Instrum. 62 (1991) 797.

[21] S.E. Gustafsson, E. Karawacki, M.A. Chohan, J. Phys. D 19 (1986) 727.

[22] M. Gustavsson, H. Wang, R.M. Trejo, E. Lara-Curzio, R.B. Dinwiddie, S.E. Gustafsson, Int. J. Thermophys. 27 (2006) 1816.

[23] S. Katlakunta, S. Singh Meena, S. Srinath, M. Bououdina, R. Sandhya, K. Praveena, Improved magnetic properties of Cr_3^+ doped $SrFe_{12}O_{19}$ synthesized via microwave hydrothermal route, Mater. Res. Bull. 63 (2015) 58–66.

[24] E.C. Stoner, E.P. Wohlfarth, A mechanism of magnetic hysteresis in heterogeneous alloys, Philos. Trans. R. Soc. A Math. Phys. Eng. Sci. 240 (1948) 599–642.

[25] Robert C. Pullar, Igor K. Bdikin b, Ashok K. Bhattacharya, Magnetic properties of randomly oriented BaM, SrM, Co2Y, Co2Z and Co2W hexagonal ferrite fibres, J. Eur. Ceram. Soc. 32 (2012) 905–913.

[26] P.G. Klemens, in: F. Seitz, D. Turnbull (Eds.), Solid State Physics, Vol. 7, Academic 1958, pp. 1–98.

[27] P.G. Klemens, Theory of the A-plane thermal conductivity of graphite, J. Wide Bandgap Mater. 7 (2000) 332–339.

[28] A. Boden, B. Boerner, P. Kusch, I. Firkowska, S. Reich, Nanoplatelet size to control the alignment and thermal conductivity in copper — graphite composites, Nano Lett. 14 (2014) 3640–3644.

[29] A. Eucken, Forsch Gebiete Ingenieurw, 1932 3.

[30] J. Francl, W.D. Kingery, Thermal conductivity: IX, experimental investigation of effect of porosity on thermal conductivity, J. Am. Ceram. Soc. 37 (1954) 99.

[31] H. Yan, Y. Tang, W. Long, et al., Enhanced thermal conductivity in polymer composites with aligned graphene nanosheets, J. Mater. Sci. 49 (2014) 5256.

[32] C. Yuan, B. Duan, L. Li, B. Xie, M. Huang, X. Luo, Thermal conductivity of polymer-based composites with magnetic aligned hexagonal boron nitride platelets, ACS Appl. Mater. Interfaces 7 (2015) 13000–13006.

[33] Y. Huang, Q. Ouyang, Q. Guo, X. Guo, G. Zhang, D. Zhang, Graphite film/aluminum laminate composites with ultrahigh thermal conductivity for thermal management applications, Mater. Des. 90 (2016) 508–515.

[34] T. Wejrzanowski, M. Grybczuk, M. Chmielewski, K. Pietrzak, K.J. Kurzydlowski, A. Strojny-Nedz, Thermal conductivity of metal-graphene composites, Mater. Des. 99 (2016) 163–173.